scientific reports

Check for updates

OPEN

Design and performance evaluation of a novel cutter-ring material based on TBM rock-breaking mechanisms

Zuliang Zhong[1]✉, Zhicheng Yang[1], Xiaoyong Li[2], Zhen Li[3] & Yiliang Tu[4]

Tunnel boring machine (TBM) disc cutters face significant challenges in complex geological conditions, particularly in composite sandstone–mudstone strata, where low rock-breaking efficiency and excessive wear affect construction efficiency and safety. To address these issues, this study first developed a cutter–rock contact model using ABAQUS, simulating stress distribution, crack propagation, and mechanical characteristics during the rock-breaking process. The simulation results confirmed the feasibility of the model, showing that stress concentration plays a key role in crack propagation, with the normal force dominating the rock-breaking process, while the rolling force acts as an auxiliary. Building on these findings, a novel cutter ring material was developed using plasma cladding technology to significantly enhance its wear resistance and impact toughness. Experimental results indicate that the new cutter ring material extends the cutter's service life by over 20%, significantly improving TBM efficiency by reducing cutter replacement frequency and maintenance costs. This research provides critical insights into cutter selection and optimization, offering a theoretical basis for improving tunneling efficiency and extending the operational lifespan of TBM cutters. The findings contribute to both theoretical advancements and practical applications in the field of tunnel boring.

Keywords Tunnel boring machine (TBM), Disc cutter rock-breaking, Numerical simulation, Sandstone, Cutter ring material

Tunnel Boring Machine (TBM) disc cutters serve as the core rock-breaking tools in tunnelling, and their cutting efficiency and cutter-ring wear characteristics are directly associated with excavation rate, maintenance cost, and construction safety. In composite strata such as sandstone–mudstone and high-strength hard rock formations, the evolution of contact stress and cutter wear at the cutter–rock interface exerts a significant influence on penetration force and rock-breaking efficiency[1,2]. Under complex geological conditions, TBM cutters frequently experience severe stress concentration, rapid crack propagation, and frequent changes in cutter-ring geometry, which collectively lead to shortened cutter life and reduced excavation efficiency[3–7]. Previous studies have demonstrated that increased cutter-ring wear rate results in a substantial rise in specific energy, intensified fluctuation of cutting forces, and more complex failure mechanisms in cutters subjected to high-impact or fissured formations[8–10]. Therefore, improving the cutting efficiency of disc cutters, extending cutter-ring service life, and optimizing cutter adaptability in complex geological conditions have become key research focuses in TBM tunnelling and cutter engineering.

To systematically grasp this issue, existing studies have conducted extensive investigations from multiple perspectives, including rock fracture mechanisms, cutter–rock interaction, cutter ring structural design and material performance, as well as cutter life prediction and engineering monitoring, and have achieved notable progress. Overall, at the level of rock mechanics, it is generally recognized that sandstone exhibits pronounced brittle fracture characteristics under cyclic loading or high-stress conditions. The failure process typically evolves through the initiation and propagation of microcracks, ultimately leading to unstable coalescence, and is accompanied by stiffness degradation and rapid energy accumulation and release. These mechanical features provide a fundamental basis for explaining crack initiation and localized sudden fragmentation during

[1]School of Civil Engineering, Chongqing University, Chongqing 400045, China. [2]Powerchina Railway Construction Investment Group Co., Ltd., Beijing 100060, China. [3]Powerchina Chengdu Electric Power Fittings Co., Ltd., Chengdu 610100, Sichuan, China. [4]School of Civil Engineering, Chongqing Jiaotong University, Chongqing 400074, China. ✉email: haiou983@126.com

disc cutter penetration[11–13]. With regard to the influence of rock-breaking efficiency and cutter structural parameters, Cheng et al.[14] systematically examined the evolution of penetration force and rock fragmentation volume under varying precut depths and confining pressures, highlighting the significant influence of free-face conditions on hard-rock fragmentation patterns. Yang et al.[15] through three-dimensional numerical simulations, investigated the cutting behavior of TBM disc cutters on microwave-pretreated basalt and showed that thermal damage substantially reduces cutting load and energy consumption. Zhou et al.[16] established a finite-element contact model between the cutter and rock, quantifying the coupled relationships among cutter geometry deformation, contact stress distribution, and crack propagation. Meanwhile, increasing attention has also been devoted to disc cutter wear behavior and structural optimization. Shin et al.[17] conducted full-scale wear tests on large-diameter shield cutters and reported that cutter-ring coatings can significantly suppress wear, although their effectiveness declines under high-impact hard-rock conditions. Su et al.[18] revealed through combined experimental–numerical approaches that cutter wear enlarges the contact area and intensifies stress concentration, thereby reducing rock-breaking efficiency and shortening cutter service life. Lyu et al.[19] proposed a sinusoidal variable-thickness cutter ring and verified that its specific energy consumption is superior to that of conventional constant-thickness rings.

In terms of wear prediction, material behavior, as well as monitoring and identification, research has gradually evolved toward the integration of multiple methods. Existing prediction models have identified key influencing factors, including installation radius, rock mass fracturing characteristics, and penetration force[20], and parameter domains aimed at mitigating impact-induced cracking have been proposed from the perspective of dynamic response[21]. Studies on material behavior and wear mechanisms indicate that excessively high-hardness materials are more susceptible to brittle fracture under water-bearing and high-impact conditions, highlighting the need to achieve a balance between wear resistance and impact toughness[22]. Meanwhile, under alternating soft–hard rock conditions, the dominant wear mode exhibits probabilistic variations[23]. On this basis, Zhang et al.[24] developed a unified model capable of simultaneously calculating wear volume, wear rate, and service life across multiple wear modes (uniform, side wear, and stepped/flat wear). In the area of monitoring and identification, Chakeri et al.[25] established an intelligent system for the identification and early warning of abnormal cutter wear, providing a data-driven auxiliary tool for field maintenance. Wang et al.[26] developed a rock rotary cutting and drilling testing system that enables systematic evaluation of the relationships among drilling parameters, rock mechanical properties, and bit structural parameters, offering valuable insights into the experimental characterization and online monitoring of cutter–rock interaction and cutter wear. With the development of machine learning techniques, many researchers have started applying data-driven approaches to enhance the accuracy of wear prediction. Ghorbani et al.[2] proposed an optimized machine learning model for predicting TBM cutter wear, achieving high-precision predictions under different lithological conditions. Li et al.[22] developed an intelligent identification and warning method for abnormal cutter wear based on Extreme Learning Machine (ELM), with the model's effectiveness in identifying and warning of abnormal wear validated through field engineering data, which is crucial for cutter maintenance and replacement planning.

Although existing studies have investigated the working behavior of disc cutters from multiple perspectives, including rock-breaking mechanisms, cutter–rock interaction, wear prediction, and cutter-ring structural design and material performance, most of these studies are conducted under single lithological conditions or idealized working scenarios. As a result, the differences in rock-breaking processes, force characteristics, and wear evolution among different cutter structural forms in composite sandstone–mudstone strata remain insufficiently understood. In particular, under conditions of frequent lithological alternation, systematic comparative analyses of the variations in contact stress distribution, crack propagation paths, and load fluctuation characteristics during cutter penetration are still lacking. Consequently, existing studies have difficulty explaining, from a structural perspective, the differences in rock-breaking efficiency and wear behavior exhibited by different cutter forms in practical engineering applications. In engineering practice, this limitation is often manifested in cutter structure selection that relies heavily on empirical judgment, making it difficult to accurately match cutter types with specific geological conditions. This mismatch can lead to reduced rock-breaking efficiency, aggravated cutter wear, and increased cutter replacement frequency in certain tunnel sections, thereby adversely affecting TBM excavation continuity and increasing construction costs. Furthermore, although the importance of material properties to cutter service performance has been widely recognized, the linkage between material design and the specific rock-breaking force characteristics remains unclear. The lack of material optimization studies grounded in rock-breaking mechanism analysis further constrains the effective application of cutter performance enhancement strategies in composite formations.

To overcome these limitations, this study investigates the strata of Region I along the University Town South Station–Zhaishanping Station section of Chongqing Rail Transit Line 27. The rock-breaking mechanisms of different cutter structural forms are systematically analyzed through combined numerical simulation and theoretical modelling. Based on the mechanistic insights into contact stress distribution, crack propagation, and fragmentation characteristics, a new cutter-ring material and corresponding manufacturing process are developed. By integrating cutter loading behavior, rock fragmentation mechanism, structural characteristics, and material performance, this study provides a theoretical foundation and technical pathway for optimizing cutter performance in composite formations, contributing to enhanced TBM excavation efficiency and prolonged cutter service life.

Engineering background

The section of Chongqing Rail Transit Line 27 between Daxuechengnan Station and Zhaishanping Station starts at Zhaishanping Station, crosses beneath the Lianhua River, and ends at Daxuechengnan Station. The mileage of the section ranges from Z(Y)DK9 + 332.315 to Z(Y)DK10 + 933.785, with the left line measuring 1,600.874 m in length and the right line measuring 1,601.470 m. The tunneling work for this section is carried out using

a composite-type tunnel boring machine (TBM). The geological profile of the shield tunneling section in this contract segment is shown in Fig. 1.

As shown in Fig. 1, the geological strata traversed by the composite TBM in the section between University Town South Station and Zhaishanping Station primarily consist of loose fill, moderately weathered sandstone, and moderately weathered mudstone. The layering of the strata in this section is quite distinct, with alternating layers of sandstone and mudstone. The mudstone layers are relatively thick and evenly distributed, making up the majority of the geological profile for this section. In contrast, the sandstone layers are intermittently distributed and relatively thin. Figure 1 also illustrates the irregular distribution of the sandstone layers, with their variation in thickness standing out in comparison to the mudstone layers. This distribution pattern indicates that the cutter will face a more complex mechanical load while passing through these strata.

During excavation in Region I of this section, significant cutter wear was observed, leading to an increase in cutter replacement frequency. The strata in this region are primarily composed of sandstone, which has a higher strength, with a saturated compressive strength ranging from 30 to 60 MPa, classifying it as hard and very hard rock. The rock mass quality is classified as Grade III. Based on the geological conditions in Region I and the observed cutter failure modes, research was conducted on the rock-breaking mechanisms of cutters in sandy and muddy strata, along with the development of new materials.

Numerical simulation of rock-breaking by disc cutters in sandstone–mudstone strata

Material model setup

Determination of disc cutter material parameters

The disc cutter is the key component of the TBM cutterhead that directly interacts with the rock, and its quality has a decisive influence on the rock-breaking performance. Therefore, when selecting the cutter ring material, it is essential that it possesses both high toughness and high hardness. A high level of hardness enables the cutter to withstand the reactive loads exerted by the rock during penetration and provides excellent wear resistance under prolonged frictional contact with the rock. Meanwhile, good toughness prevents brittle fracture caused by the impact of rock debris and helps reduce vibrations induced by lateral forces and uneven loading.

In the numerical simulation, the cutter ring material was modeled as a linear elastic material, considering that its deformation is negligible compared with that of the surrounding rock. The mechanical parameters of the cutter ring used in the model are listed in Table 1.

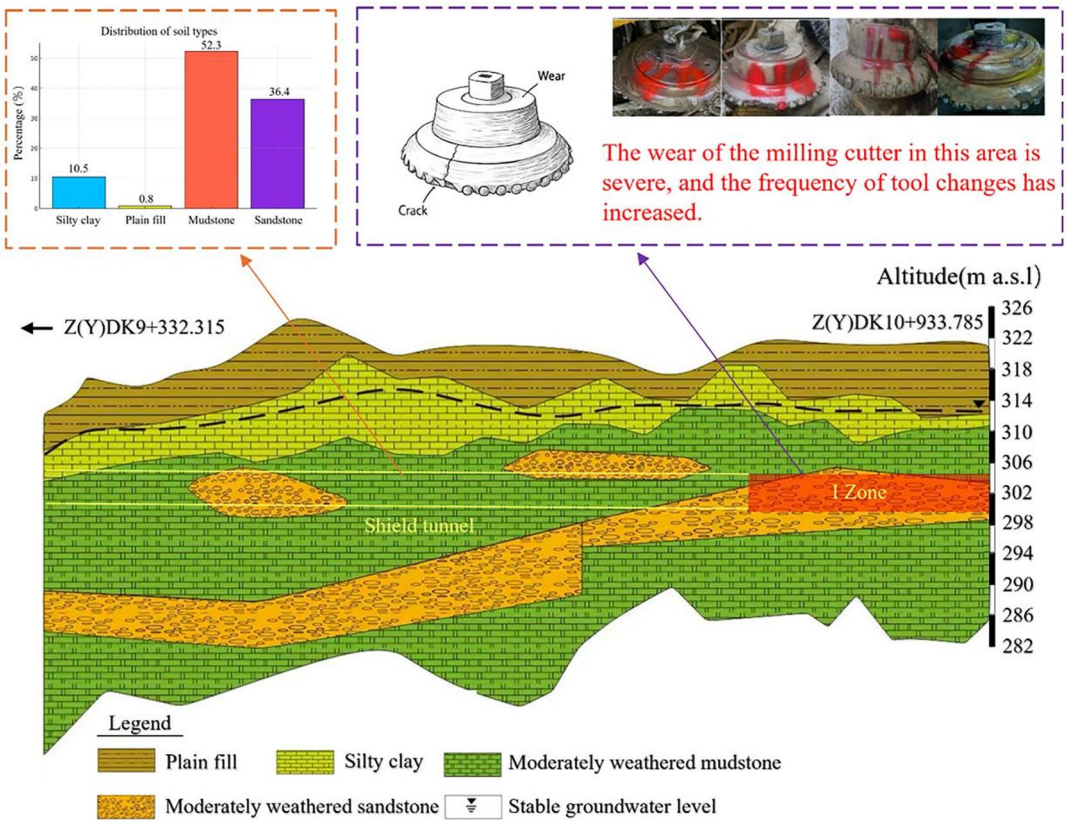

Fig. 1. Geological cross-section of the study area.

Density (kg/m³)	Elastic modulus (GPa)	Poisson's ratio
7900	210	0.3

Table 1. Cutter ring material parameters.

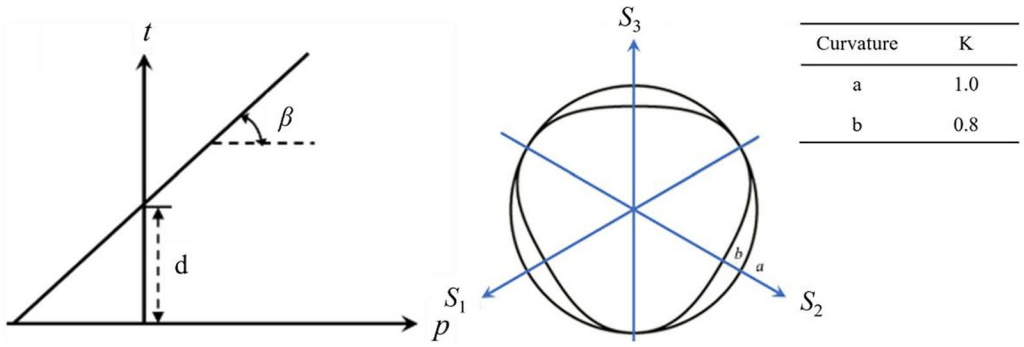

Fig. 2. Yield surface of the Drucker–Prager (D–P) model.

Type	Density (kg/m³)	Elastic modulus (GPa)	Poisson's ratio	Cohesion (MPa)	UCS (MPa)	UTS (MPa)
Sandstone	2580	12.83	0.17	8	65.73	3.44
Mudstone	2800	16.29	0.26	10	13.83	2.18

Table 2. Demonstrate the mechanical parameters of the model material.

Rock constitutive model and determination of material parameters

ABAQUS, with its powerful finite element analysis capabilities, comprehensive constitutive models for geotechnical materials, and advanced post-processing functions, is widely applied in civil and geotechnical engineering for accurately simulating the mechanical behavior of rocks. Considering the complexity of rock mechanical responses, this study adopts the Drucker–Prager (DP) yield criterion to describe the plastic constitutive behavior of the rock material[27]. This criterion features a simple mathematical form, clear physical meaning of parameters, and the ability to account for the effects of hydrostatic pressure and the intermediate principal stress. Numerous studies have confirmed its effectiveness in modeling rock fragmentation processes under disc cutter loading.

In this study, a linear Drucker–Prager model is employed, and the corresponding yield surface is illustrated in Fig. 2. The yield criterion can be expressed as follows:

$$F = t - p\tan\beta - d = 0 \tag{1}$$

$$t = \frac{q}{2}\left[1 + \frac{1}{k} - \left(1 - \frac{1}{k}\right)\left(\frac{r}{q}\right)^3\right] \tag{2}$$

where t is the deviatoric stress (kN), p is the equivalent compressive stress (kN), β is the inclination angle of the yield surface in the stress space (°), d is the material cohesion (kPa), k denotes the ratio of triaxial tensile strength to triaxial compressive strength, q represents the Mises equivalent stress (kPa), and r is the third invariant of the deviatoric stress (kPa).

The material parameters of the rock model were determined based on the measured values obtained from the Daxuechengnan Station–Zhaishanping Station section of Chongqing Rail Transit Line 27, as presented in Table 2.

Model construction and mesh generation

The cutterhead of a shield TBM breaks the rock through the action of disc cutters. The cutter ring, which is the critical component directly contacting the rock, is made of a high-strength brittle material and can therefore be simplified as a linear elastic body in the numerical model[28]. This simplification is based on the fact that the cutter ring primarily experiences elastic stresses during the rock-breaking process, and the material's plastic deformation and fatigue effects are relatively minor during the initial fracture stage. Therefore, using a linear elastic model in the analysis of cutter ring performance helps capture the primary mechanical behavior of early crack propagation. In this study, a commonly used 17-inch disc cutter was selected to investigate rock fragmentation under cutter loading. The cutter specifications are as follows: outer diameter of 432 mm, inner

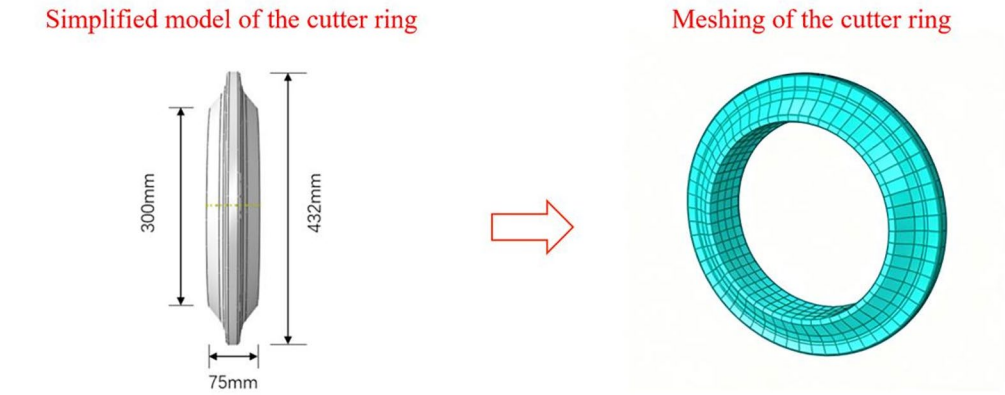

Fig. 3. Numerical model of the disc cutter ring.

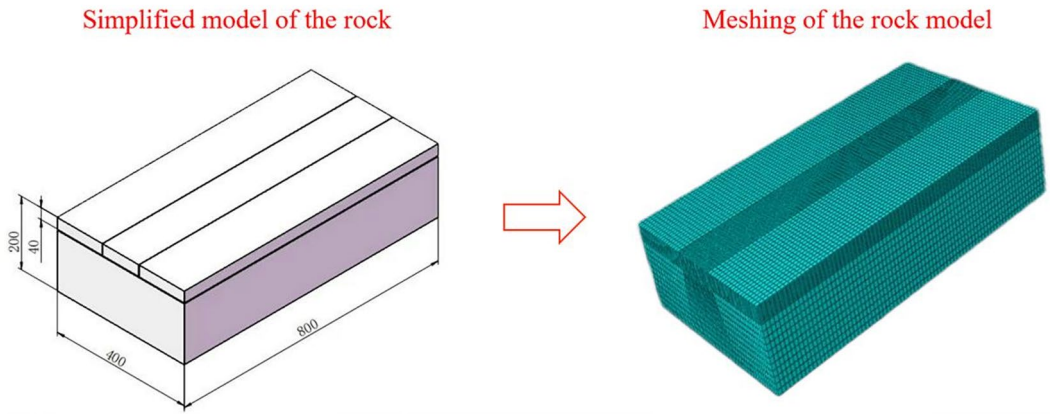

Fig. 4. Numerical model of the rock.

diameter of 300 mm, linear blade width of 17.5 mm, blade angle of 20°, cutter ring thickness of 75 mm, and transition radius of 3.5 mm.

In the numerical simulation, the disc cutter was discretized using C3D8R eight-node reduced-integration hexahedral elements, with a mesh size of 20 mm, resulting in a total of 1,740 elements. The simplified cutter model and the corresponding mesh configuration are shown in Fig. 3.

As shown in Fig. 4, the dimensions of the rock specimen are $800 \times 400 \times 200$ mm. During the rolling–crushing process, the rock in direct contact with the cutter blade and the surrounding region is subjected to highly concentrated stresses. Considering both computational efficiency and simulation accuracy, the rock model was divided into two layers, with the upper layer having a thickness of 40 mm.

The mesh configuration is arranged such that the upper layer is discretized with an element size of 4 mm, while the lower layer is meshed with an element size of 16 mm. Both layers were modeled using reduced-integration hexahedral elements (C3D8R), with element deletion enabled. The total number of rock elements in the model is 105,840.

Analysis steps, contact definition, and interaction settings

The rock-breaking process induced by the disc cutter is highly dynamic and nonlinear, and the contact behavior between the cutter ring and the rock is difficult to describe accurately. The Explicit module in ABAQUS employs a central-difference explicit time integration scheme, which dynamically adjusts the subsequent time increments according to the computational response, making it particularly suitable for highly nonlinear contact problems.

In the analysis step configuration, ABAQUS automatically includes an initial step. In this step, the bottom surface of the rock model is fully constrained, and normal constraints are applied to the two side faces along the longitudinal direction. In addition to the initial step, a *penetration step* and a *rolling step* are defined. The penetration step simulates the downward intrusion of the cutter into the rock, with a penetration duration of 0.1 s. The rolling step simulates the subsequent rolling process after the cutter reaches the predetermined penetration depth. The duration of this step is 1 s, with a rolling linear velocity of 800 mm/s and an angular velocity of 3.704 rad/s.

General contact is adopted in the interaction settings. The normal behavior is defined as "hard contact," while the tangential behavior follows a "penalty" formulation with a friction coefficient of 0.3.

Boundary conditions of the finite element model

As illustrated in Fig. 5, the rock specimen is positioned at the center of the base plate with full contact. The base plate surface is fully constrained (indicated by the blue arrows), restricting all translational degrees of freedom. The loading device above the specimen consists of a circular rigid ring, which is coupled to a reference point (RP-1) located at the ring center. Moreover, the entire rock base plate is defined as a rigid body and coupled to another reference point (RP-2), where all translational and rotational degrees of freedom are constrained during the dynamic analysis.

The loading procedure is applied through RP-1, including vertical loading, lateral loading, and rotational motion around the ring axis. This configuration enables the application of compound loading conditions to the rock specimen. The boundary condition design of this study mainly focuses on the mechanical process of rock cutting by the cutter. To simplify the simulation and concentrate on the rock fracture behavior under the action of the cutter, this model does not consider the effects of dynamic environmental factors such as groundwater and temperature. Although these factors may influence the rock fracture process in real-world engineering, the core goal of this study is to simulate the interaction between the cutter and the rock, studying the stress and fracture mechanisms of the rock. Therefore, these factors were not incorporated into the model.

Validation of numerical simulation results

CSM prediction model

Rostami[29] integrated the theories of compressive, shear, and tensile rock failure and proposed the widely accepted CSM model for predicting disc cutter forces. The model comprehensively considers both the mechanical properties of rock materials and the structural parameters of disc cutters. As a result, the cutter force predictions obtained using the CSM model are much closer to field measurements in engineering practice, demonstrating strong applicability and reliability.

$$F_T = \int_0^{\phi} TRpd\theta = \int_0^{\phi} TRp_0 \left(\frac{\theta}{\phi}\right)^{\psi} d\theta = \frac{TRp_0\phi}{1+\psi} \tag{3}$$

$$\phi = \cos^{-1}\left[(R-h)/R\right] \tag{4}$$

where P_0 is the base pressure within the rock fragmentation zone, which is related to the rock strength and the structural parameters of the disc cutter. Through extensive linear cutting tests and regression analysis of the obtained data, Rostami eventually established the empirical expression for P_0 as follows:

$$p_0 = C\sqrt[3]{\frac{S\sigma_C^2\sigma_t}{\phi\sqrt{RT}}} \tag{5}$$

In the equation, C is generally taken as 2.12 and represents a dimensionless coefficient indicating the ratio between the rolling force and the normal force of the disc cutter; S denotes the cutter spacing; σ_c is the uniaxial compressive strength of the rock; and σ_t is the tensile strength of the rock.

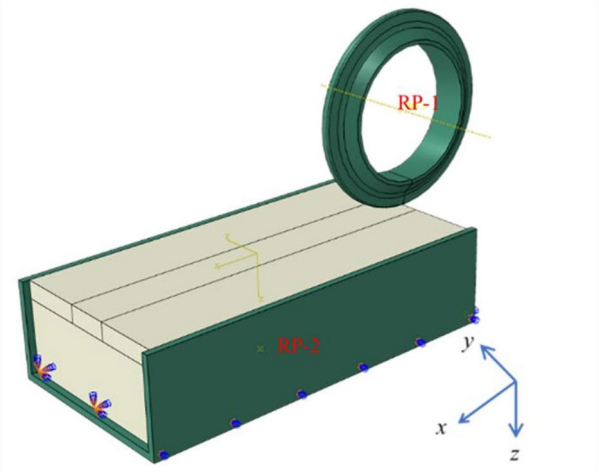

Fig. 5. Boundary condition settings.

In this way, the resultant force acting on the disc cutter during rock fragmentation can be determined, and the normal force and rolling force of the cutter can be obtained through force decomposition as follows:

$$F_V = F_T \cos\frac{\phi}{2} = \frac{TRp_0\phi}{1+\psi}\cos\frac{\phi}{2} \tag{6}$$

$$F_R = F_T \sin\frac{\phi}{2} = \frac{TRp_0\phi}{1+\psi}\sin\frac{\phi}{2} \tag{7}$$

Establishment of the rock-breaking force prediction model

The CSM model comprehensively considers rock strength, cutter tip structural parameters, cutter spacing, and penetration depth, among other factors. However, the traditional CSM model treats the cutter tip width as a constant and does not adequately account for the changes caused by cutter wear during actual tunneling[30]. As penetration depth increases, the actual contact width between the cutter tip and the rock also increases, yet the traditional model cannot effectively reflect this change.

To address this limitation, the effects of cutter wear and penetration depth on the actual contact width were fully considered in this study, and the traditional CSM model was modified accordingly. A wear-based cutter force prediction model was developed, with the core concept being to retain the mechanical framework of the CSM model while introducing an equivalent cutter width $b_{\text{eff}} = b_0 + w$, where w represents the wear-induced increase. This allows the cutter force expressions to incorporate the "wear–geometry–loading" coupling mechanism.

(1) Simplification of the cutter tip geometry.

According to Gertsch and colleagues at the Colorado School of Mines, full-scale linear cutting tests have shown that the cutter tip gradually wears down and becomes flattened during the rock-cutting process, forming a plano-convex contact surface[31]. Therefore, the contact profile between the worn cutter tip and the rock can be approximated as a combination of a plane and an elliptical contact region. The major and minor semi-axes of the contact area can thus be expressed as:

$$l_c = \sqrt{2Rh}, \quad b_{eff} = b_0 + w \tag{8}$$

where l_c is the contact length (major semi-axis), b_{eff} is the effective contact width (minor semi-axis), R is the cutter radius, h is the penetration depth, b_0 is the initial cutter tip width, and w is the wear-induced increment[31].

(2) Derivation of the rock-breaking force prediction model.

(1) Calculation of the base pressure.

Based on the results of the CSM model, the base pressure within the rock fragmentation zone can be expressed as follows:

$$p_b = C_0(\sigma_c)^m(\sigma_t)^n\left(\frac{s}{R}\right)^{\eta}\left(\frac{h}{R}\right)^{\xi} \tag{9}$$

where C_0 is the empirical coefficient; σ_c and σ_t are the uniaxial compressive strength and tensile strength of the rock, respectively; s is the cutter spacing; and m, n, η, and ξ are empirical indices[30].

As shown in Fig. 6, during the indentation process of the disc cutter, the pressure distribution at the contact interface between the cutter tip and the rock follows a Hertzian distribution[30]. The stress at each contact point is always oriented normal to the rock-breaking surface, enabling an accurate analysis of the cutter–rock interaction at the microscale. Based on the relationship between action and reaction forces, the corresponding rock-breaking

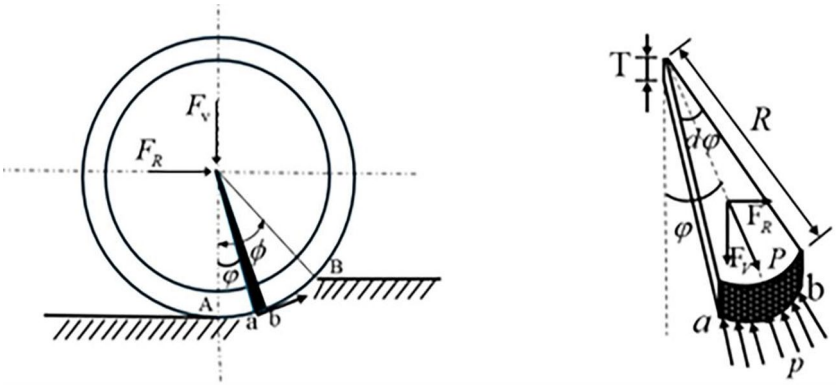

Fig. 6. Schematic of the resultant force and its components on a differential element.

force exerted on the cutter can be derived. According to Hertzian contact theory, the peak contact pressure on the interface can be expressed as:

$$p_0 = \alpha_H p_b \tag{10}$$

where α_H is the Hertzian contact correction coefficient[30].

(2) Calculation of normal cutting force.

According to the elliptical contact integration theory, the normal cutting force F_v can be expressed as:

$$F_v = \frac{\pi}{3} p_0 b_{eff} l_c \tag{11}$$

By substituting Eqs. (6) and (8) into the above expression, we obtain:

$$F_v = \frac{\pi}{3} \alpha_H C_0 (\sigma_c)^m (\sigma_t)^n \left(\frac{s}{R}\right)^\eta \left(\frac{h}{R}\right)^\xi (b_0 + w)\sqrt{2Rh} \tag{12}$$

(3) Calculation of rolling force.

The relationship between the rolling force F_n and the normal force F_v can be determined according to the frictional conditions.

$$F_n = \mu_{eff} F_v \tag{13}$$

where μ_{eff} is the effective friction coefficient[32]. Considering the effect of abrasive wear, it can be approximated linearly as:

$$\mu_{eff} = \mu_0 + k_\mu w \tag{14}$$

where μ_0 is the initial friction coefficient, k_μ is the friction correction coefficient, and w is the wear amount[32].

(4) Wear evolution equation.

Based on Archard's wear law[33], and considering the effects of load and wear saturation, the evolution of wear can be expressed as:

$$\dot{w} = \frac{2k_A}{3H} \alpha_H p_b v - \kappa_w w \tag{15}$$

where k_A is the wear coefficient, H is the hardness of the cutter ring material, v is the cutting velocity of the disc cutter, and κ_w is the wear attenuation coefficient[34].

By integrating Eq. (13), an analytical solution can be obtained as follows:

$$w(t) = \frac{2k_A}{3H} \frac{\alpha_H p_b v}{\kappa_w} \left(1 - e^{-\kappa_w t}\right) \tag{16}$$

(5) Final derivation.

By substituting the wear evolution result $w(t)$ into Eqs. (10) and (11), the rock-breaking forces of the disc cutter considering the wear effect can be obtained.

The final predictive formulas for the cutting forces are given as follows:

$$F_v(t) = \frac{\pi}{3} \alpha_H C_0 (\sigma_c)^m (\sigma_t)^n \left(\frac{s}{R}\right)^\eta \left(\frac{h}{R}\right)^\xi \left[b_0 + \frac{2k_A}{3H} \frac{\alpha_H p_b v}{\kappa_w} \left(1 - e^{-\kappa_w t}\right)\right] \sqrt{2Rh} \tag{17}$$

$$F_n(t) = \mu_{eff} F_v(t) \tag{18}$$

Theoretical verification of numerical simulation results

The force states of the disc cutter cutting sandstone and mudstone are shown in Figs. 7 and 8, respectively. It can be observed that the disc cutter exhibits a chipping-type (jumping) rock-breaking behavior when cutting both types of rock. Moreover, the rolling force of the cutter is approximately one-tenth of the normal force[31].

To verify the reliability of the numerical simulation results, the numerical simulation results were cross-validated with the cutting force prediction model based on wear and field experimental results. The comparison results are shown in Table 3. For sandstone, the cutter numerical simulation results were similar to those of the prediction model. The normal force was 3.26 kN smaller than the calculated value, with a relative error of 3.01%,

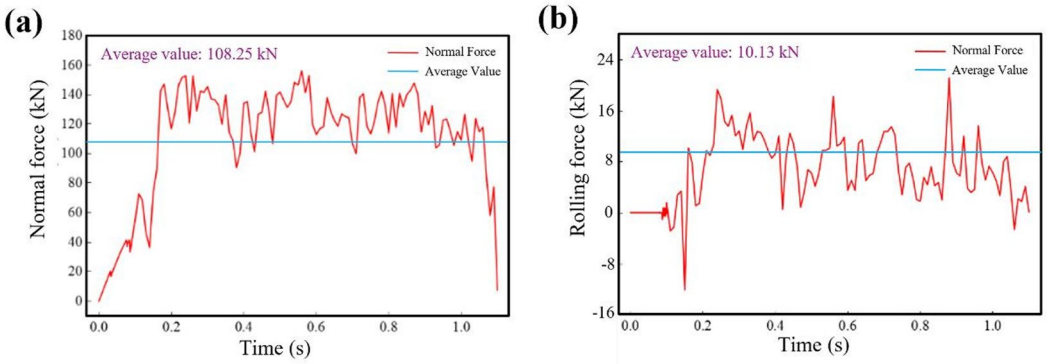

Fig. 7. Force state during disc cutter cutting of sandstone: (**a**) Normal force during disc cutter cutting of sandstone, (**b**) Rolling force during disc cutter cutting of sandstone.

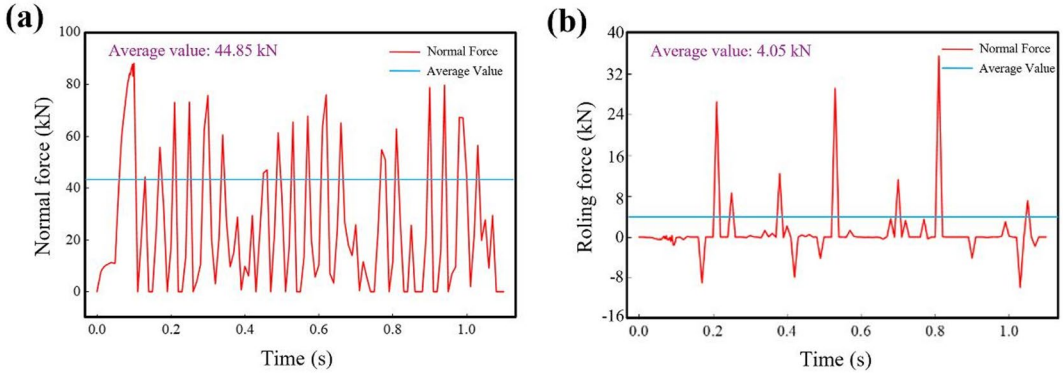

Fig. 8. Force state during disc cutter cutting of mudstone: (**a**) Normal force during disc cutter cutting of mudstone, (**b**) Rolling force during disc cutter cutting of mudstone.

	Numerical simulation results (kN)		Calculated results (kN)		Experimental results (kN)	
Lithology	Normal force	Rolling force	Normal force	Rolling force	Normal force	Rolling force
Sandstone	108.25	10.13	111.51	10.58	107.50	9.65
Mudstone	44.85	4.05	47.18	4.16	46.30	4.15

Table 3. The force of the hob breaking rock.

and the rolling force was 0.65 kN smaller than the calculated value, with a relative error of 4.44%. Compared with the experimental data, the normal force error was 0.75 kN, with a relative error of 0.7%, and the rolling force error was 0.48 kN, with a relative error of 5.0%. For mudstone, the cutter numerical simulation normal force was 2.33 kN smaller than the prediction model, with a relative error of 5.19%, and the rolling force was 0.11 kN larger than the calculated value, with a relative error of 2.72%. Compared with the experimental data, the normal force error was 1.45 kN, with a relative error of 3.11%, and the rolling force error was 0.1 kN, with a relative error of 2.41%.

Overall, in terms of relative magnitude, the maximum error between the numerical simulation results and the calculated values is 5.19%, while the maximum error with the experimental results is 5.0%. Regarding the cutter force characteristics, all specimens exhibited a stepwise fragmentation pattern, which is consistent with the actual engineering conditions. Combining the error analysis, it is evident that the numerical simulation results not only align with the predictions of the calculation model but also validate the consistency between the numerical simulation results and the field experimental data. These two aspects demonstrate the feasibility of the model in simulating cutter rock-breaking results.

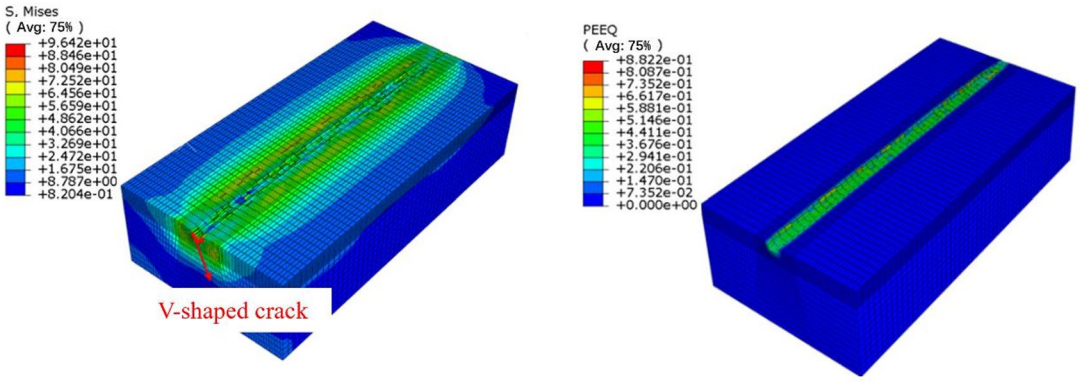

Fig. 9. Fragmentation state of sandstone during disc cutter cutting.

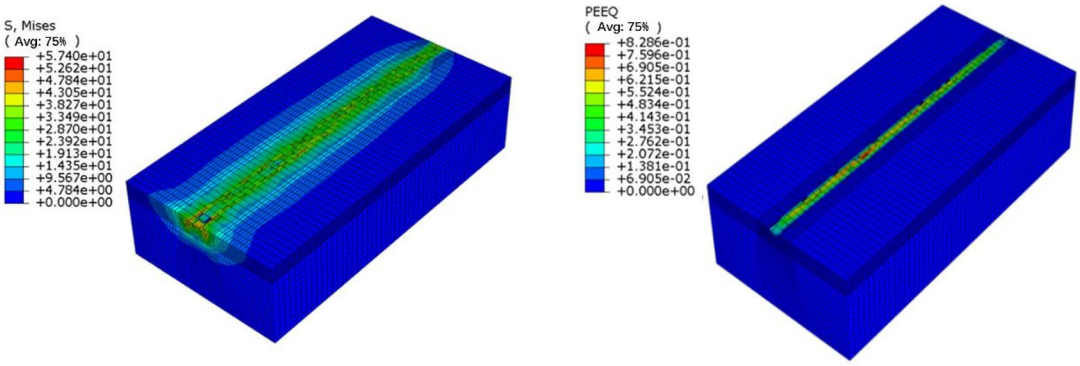

Fig. 10. Fragmentation state of mudstone during disc cutter cutting.

Influence of different cutter types on rock-breaking performance

Influence of smooth-edge cutters on the fracturing characteristics of different rocks

The section between Daxuechengnan Station and Zhaishanping Station on Chongqing Rail Transit Line 27 consists mainly of interbedded sandstone and mudstone, exhibiting significant lithological differences, including both moderately hard rock layers and soft–plastic layers. The smooth-edge cutter is the most commonly used and widely adaptable cutter type in TBM tunneling, and it can represent the fundamental rock-breaking characteristics under various lithological conditions.

Therefore, this subsection selects sandstone and mudstone as two typical strata to numerically simulate the rock-breaking mechanism of the smooth-edge cutter. The purpose is to analyze the influence of lithological variation on cutter force characteristics and rock fragmentation behavior, thus providing a fundamental comparison basis for subsequent structural improvement. The fractured states after cutting sandstone and mudstone are shown in Figs. 9 and 10, respectively.

Through observation of the Mises stress contour maps, it can be seen that significant stress concentration occurs in the area where the cutter first contacts the rock. Additionally, the color changes in the Mises stress contour map indicate that the stress increases closer to the cutter, implying that the reactive force on the rock is greater near the cutter region. The stress map also reveals the crack propagation. The smooth-edge cutter, due to its continuous contact surface, results in a more uniform stress distribution during the rock-breaking process. As a result, the crack propagation rate is slower and tends to follow the more evenly distributed stress regions, exhibiting stable propagation characteristics. Furthermore, by comparing the fracture states of sandstone and mudstone, it is evident that sandstone undergoes more significant fragmentation, indicating that the rock lithology plays a considerable role in determining the extent of fragmentation under cutter action[35].

As shown in Fig. 9, cracks are generated beneath the cutter due to the rolling and compressive action, forming a V-shaped crack profile. The rock-breaking forces experienced by the cutter can be generally divided into three stages (in reference to Figs. 7, 8). The first stage occurs from 0 to approximately 0.1 s, during which the cutter contacts and indents the rock, and the cutter load begins to increase. The second stage spans from 0.1 to 1.1 s, representing the stable cutting phase, during which both the normal force and the rolling force exhibit a sawtooth pattern fluctuating around their mean values. The third stage occurs between 1.1 and 1.2 s, as the cutter approaches the edge of the rock block and gradually disengages from the rock mass, causing the cutter forces to progressively decrease to zero.

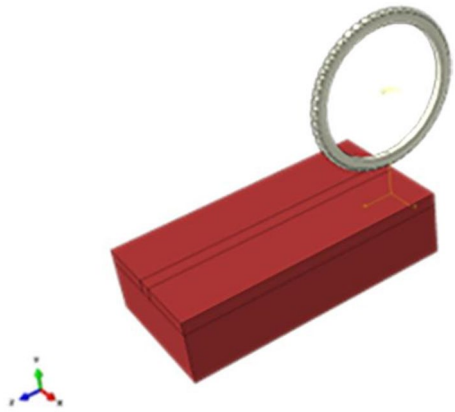

Fig. 11. Assembly diagram of the inserted-tooth disc cutter.

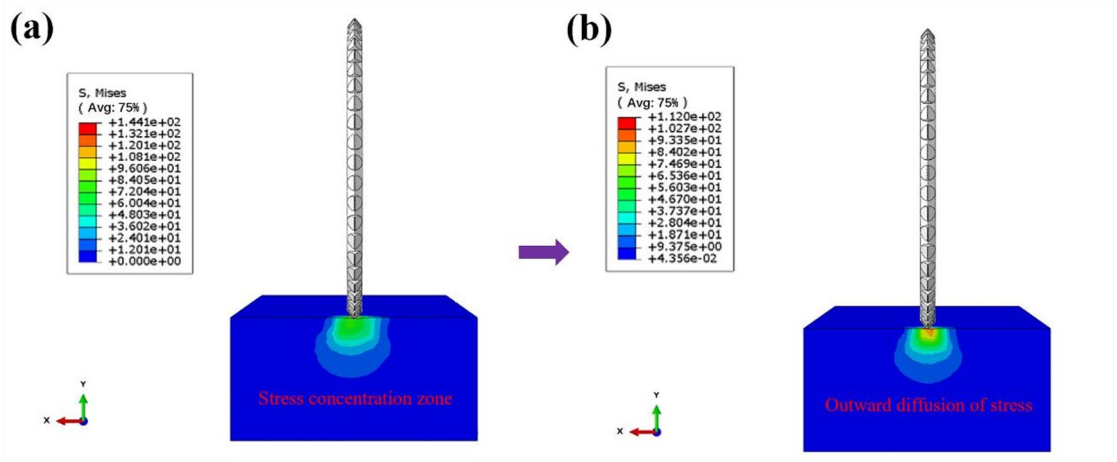

Fig. 12. Diagram of the rock fragmentation process: **a** the occurrence of stress blisters, **b** the outward radiation and transmission of stress.

Influence of single-edge insert cutters on rock-breaking performance

In the section between Daxuechengnan Station and Zhaishanping Station of Chongqing Rail Transit Line 27, a composite TBM is used for construction, and all cutters on the cutterhead are insert-type disc cutters. Since the strata in Region I consist mainly of sandstone with high strength and abrasiveness, insert cutters—commonly applied in moderately hard and highly abrasive rock—are selected. However, their cutting advantage is not significant in soft mudstone. Therefore, the TBM cutterhead adopts insert cutters exclusively. Meanwhile, to reveal the actual rock-breaking behavior in this region, the numerical simulation of insert cutters is conducted only under sandstone conditions.

The single-edge insert cutter is primarily arranged in the inner region of the cutterhead, designed with a single cutting edge to concentrate cutting forces. Due to the geometric complexity of the arcuate inserts and their mounting structures, this study employs tetrahedral elements to discretize the insert cutter ring. After meshing, a total of 7,581 finite elements are generated. To balance computational accuracy and efficiency, the cutter is simplified as a rigid body during numerical simulation. Detailed information on the assembly structure is shown in Fig. 11.

In the initial stage of contact between the single-edge insert cutter and the rock mass, the first row of carbide inserts engages the rock surface and begins the rock-breaking process. At this moment, as the stress gradually increases, pre-existing micro-cracks within the rock start to close, and local stress concentration zones begin to form (as shown in Fig. 12a). With the cutter further penetrating into the rock, the indentation depth continues to increase, leading to a corresponding rise in stress levels. The stress concentration zone gradually expands outward, and a compacted core is progressively formed. The region directly in contact with the cutter tip exhibits higher and more concentrated stresses, radiating outward from the contact zone (as shown in Fig. 12b).

Subsequently, as the penetration continues, the stress further increases, and the rock elements directly beneath the cutter tip reach the damage threshold first. Element deletion occurs, corresponding to the detachment of rock chips. At this moment, the cutter temporarily loses contact with the rock surface, resulting in a sharp drop in cutter load. During the rock-breaking process, as the carbide inserts on the disc cutter continuously indent

the rock formation, the load acting on the cutter increases. When the insert tip fully penetrates the rock in the normal direction, both the penetration depth and the cutting force reach their maximum values and then begin to decrease simultaneously.

Once the stress at the insert tip exceeds the rock's failure threshold, brittle fracturing occurs in the rock surrounding the indentation zone, resulting in a stepwise drop in cutting force. With the continuous rotational movement of the cutter, the insert tip undergoes a cyclic "indentation–withdrawal" process within the rock mass, causing the cutting force to exhibit pronounced oscillatory behavior. Meanwhile, under the action of the single-edge insert cutter, the effect of localized stress concentration is particularly pronounced. When the cutter teeth contact the rock, cracks typically propagate rapidly along the stress concentration regions, forming irregular crack paths. This is due to the uneven stress distribution caused by the geometry of the cutter teeth, leading to intense localized failure in the rock. Through the crack propagation trajectories observed in numerical simulations, it can be seen that cracks primarily extend along the direction of cutter tooth contact rather than along more uniformly distributed stress regions. This indicates that the cutter tooth geometry is closely related to the crack propagation path in the rock, with the propagation path exhibiting strong directional characteristics. Furthermore, compared to the smooth-edge cutter, the single-edge insert cutter exhibits a faster crack propagation rate, suggesting that the stress concentration induced by the cutter tooth geometry accelerates crack growth.

The variations of normal force and rolling force during the linear cutting process of the single-edge insert cutter are shown in Fig. 13. During rock cutting, the vertical force acting on the insert cutter exhibits a pronounced periodic characteristic[36], and this periodicity is even more evident than that observed in Fig. 7. The geometric structure of the single-edge insert cutter causes localized stress concentrations during cutting, as each cutter tooth induces stress concentration when it contacts the rock. Under this structure, each tooth causes substantial stress concentration and triggers significant force fluctuations. These force fluctuation characteristics primarily result from the contact mode between the cutter tooth and the rock. Each time a tooth penetrates the rock, the periodic variation between the cutting force and the release force causes an increase in the amplitude of the force curve fluctuations. Compared to the smooth-edge cutter, the single-edge insert cutter exhibits a higher amplitude of force fluctuations and greater cutting resistance.

In combination with the analysis in Sect. "Influence of smooth-edge cutters on the fracturing characteristics of different rocks", both the smooth-edge cutter and the single-edge insert cutter exhibit a jump-like fragmentation pattern during the rock-breaking process. In both cases, the rolling force is significantly smaller than the normal force, indicating that the rock-breaking behavior is primarily governed by the normal force, while the rolling force, although relatively small, still contributes and cannot be neglected. The region where the cutter initially contacts the rock shows clear stress concentration, and the stress magnitude increases with proximity to the cutter. As the cutter penetrates deeper, cracks begin to initiate near the contact zone and gradually propagate outward. This demonstrates that cutter penetration is the key factor triggering the initiation and propagation of internal cracks, which subsequently lead to rock fragmentation.

The rock-breaking processes of both cutter types can generally be divided into three stages. The first stage corresponds to the initial contact and compression between the cutter and the rock, during which the cutter load begins to increase. The second stage represents the stable cutting phase, during which the normal and rolling forces fluctuate. In the third stage, the cutter approaches the boundary of the rock block and gradually moves away from the rock mass, causing the cutter forces to diminish to nearly zero. These stage characteristics reflect the evolving interaction between the cutter and the rock under varying cutter positions and penetration depths.

Influence of double-edge insert cutters on rock-breaking performance

Double-edge insert cutters are mainly arranged in the outer annular region of the cutterhead. Each cutter is equipped with a dual-edge design that enhances cutting efficiency and reduces wear by ensuring a more uniform distribution of cutting forces. In contrast, double-edge smooth-edge cutters are seldom used in the Chongqing area. Their rock-breaking mechanism is similar to that of single-edge smooth-edge cutters, but their advantages cannot be fully realized in abrasive sandstone formations, resulting in limited engineering applicability. Therefore,

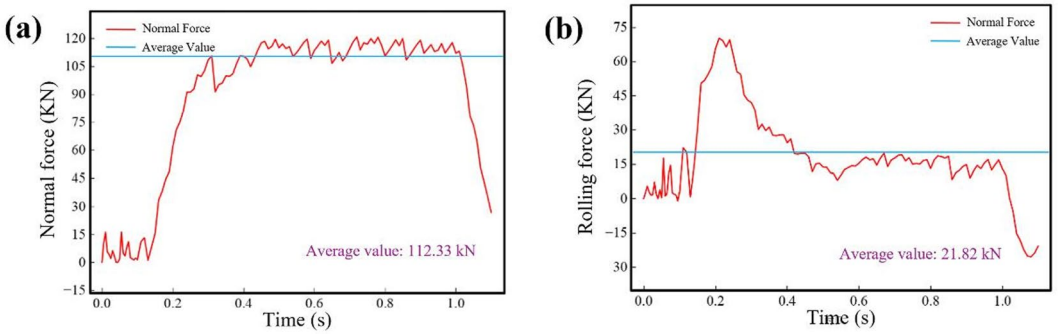

Fig. 13. Load variation curve of the inserted-tooth disc cutter during rock cutting: **a** the normal force during disc-cutter rock breaking, **b** the rolling force during disc-cutter rock breaking.

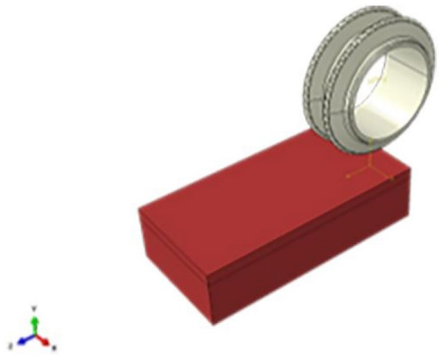

Fig. 14. Schematic diagram of the assembly of a double-edged inserted-tooth disc cutter.

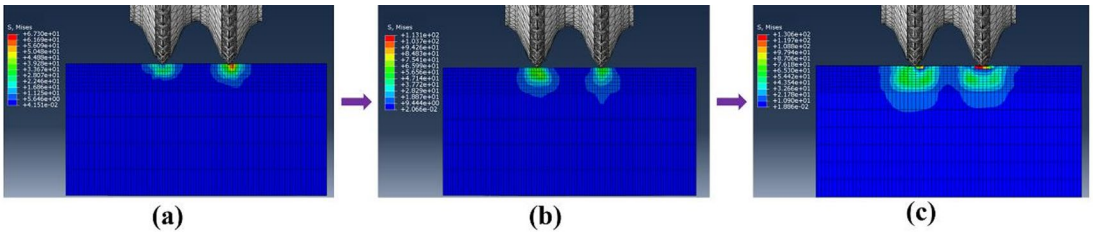

Fig. 15. Schematic diagram of the rock-breaking process of a double-edged inserted-tooth disc cutter: (**a**) Microcrack initiation stage, (**b**) Compacted core formation stage, **c** Lateral crack propagation stage.

they are not included in the present study. The assembly of the double-edge insert cutter with sandstone is shown in Fig. 14.

The rock-breaking process of the double-edge insert cutter is shown in Fig. 15. According to the color gradient patterns of the stress contour, it can be observed that during the penetration stage, a "U-shaped" stress distribution forms within the rock region in contact with the cutter. The closer the area is to the cutter's rolling zone, the darker the stress contour becomes, indicating higher stress levels. In contrast, areas farther away from the cutter exhibit gradually decreasing influence, with the contour shifting toward blue, representing low-stress regions that have not yet been affected by the cutter's rock-breaking action. The rock-breaking process of the double-edge cutter can be generally divided into three stages: the microcrack initiation stage, the compaction core formation stage, and the lateral crack development stage[37].

Microcrack initiation stage: After the cutter penetrates and contacts the rock, a stress bulb forms beneath the cutter. The region in direct contact with the cutter tip experiences the highest stress. When the stress on the rock beneath the cutter tip exceeds the rock strength, microcracks begin to initiate (see Fig. 15a).

Compaction core formation stage: As the cutter penetrates further, the pre-existing microcracks within the rock become compacted under the cutter load, forming a compaction core beneath the cutter. This core continues to act as the medium for stress transmission, allowing the cutter load to be transferred deeper into the rock mass (see Fig. 15b).

Lateral crack development stage: With continued penetration, the compaction core expands, and lateral cracks begin to develop around its boundary. Consequently, the crushed zone beneath the cutter enlarges further (see Fig. 15c).

The rock-breaking effect of the double-edge insert cutter is shown in Fig. 16. During the rolling stage, the rock located immediately ahead of the cutter tip experiences the highest stress, making it the most vulnerable region to damage. As rolling progresses, the rock on both sides of the cutter continuously accumulates stress due to the cutter's rolling action, gradually forming a distinct influence zone. This process continues until the rock within this zone fails due to excessive stress. Throughout the rock-breaking process, the rock mass is subjected to continuous compressive loading from the cutter, and the region experiencing the maximum stress is the critical zone governing the onset of rolling-induced failure.

As the cutter advances, the stress within the rock progressively accumulates until it reaches the failure threshold. When elements along the cutting trajectory reach their failure displacement, the corresponding elements are removed. After deletion, the stress in that region instantaneously drops to zero. Consequently, with the continuous forward motion of the cutter, the location of maximum stress shifts forward accordingly, always remaining near the leading edge of the cutter tip along its motion path. As shown in Fig. 16, it can be observed that cracks primarily propagate along the contact area of the cutter teeth. As the cutter penetrates deeper into the rock, the cracks gradually extend outward, ultimately leading to rock fragmentation. The geometric structure of the double-edge insert cutter accelerates crack propagation, making the fragmentation process more intense compared to the single-edge insert cutter. The crack propagation path is no longer a simple extension

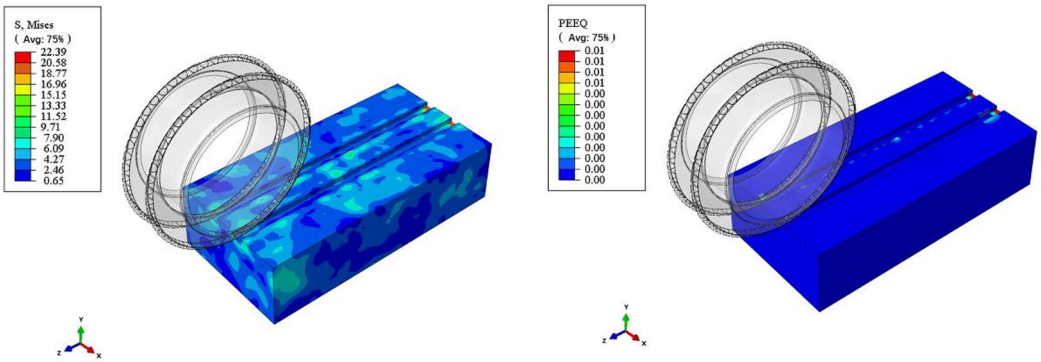

Fig. 16. Rock fragmentation effect diagram: (**a**) the normal force during disc-cutter rock breaking, (**b**) the rolling force during disc-cutter rock breaking.

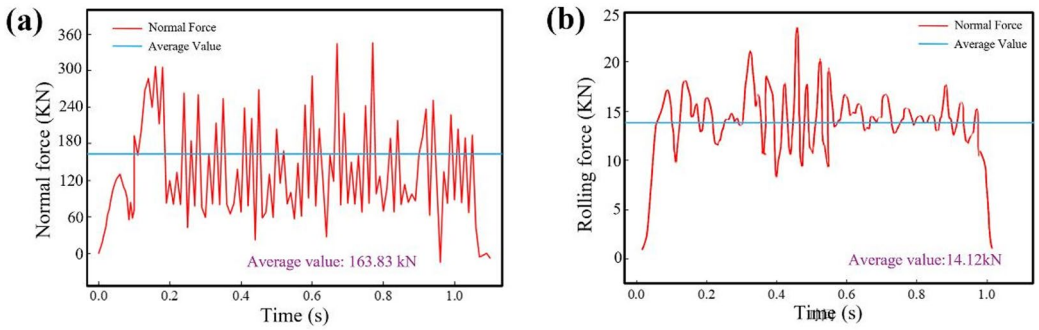

Fig. 17. Load variation curve of the double-edged inserted-tooth disc cutter during rock cutting: (**a**) the normal force during disc-cutter rock breaking, (**b**) the rolling force during disc-cutter rock breaking.

along the stress concentration regions but forms a more complex propagation pattern. Cracks exhibit jump-like propagation between different stress regions, resulting in a more intricate fragmentation mode. Compared to the smooth-edge cutter and single-edge insert cutter, the double-edge insert cutter exhibits a faster crack propagation rate. The dual cutting action of the cutter teeth causes more intense stress concentration, resulting in faster and more complex crack propagation and fragmentation processes.

The time-history curves of the normal force and rolling force of the double-edge insert cutter are shown in Fig. 17. The normal and rolling force curves of the double-edge cutter still exhibit jump-like and fluctuating characteristics. By comparing these results with those in Fig. 13, it can be observed that under the same rock-breaking conditions, the average normal force and fluctuation amplitude of the double-edge insert cutter are both greater than those of the single-edge insert cutter. This is because the dual-edge configuration induces stronger stress superposition and more complex fracture responses when both edges engage the rock simultaneously. However, the average normal force of the double-edge cutter is less than twice that of the single-edge cutter, which is attributed to the facilitating effect of adjacent cutter edges on the rock-breaking process.

In contrast, the single-edge insert cutter exhibits a larger average rolling force and greater fluctuation amplitude, mainly because its shear and frictional actions are more concentrated, resulting in more pronounced resistance in the rolling direction. Overall, the double-edge insert cutter experiences higher normal loads with more intense fluctuations, whereas the single-edge cutter is characterized by larger tangential loads and more significant rolling vibrations.

Development of a new cutter ring based on rock-breaking characteristics

Influence of rock-breaking mechanics on cutter ring design

Through numerical simulation of the rock-breaking mechanism in the Cutter Zone I section between University Town South Station and Zhaishanping Station along Chongqing Rail Transit Line 27, the mechanical characteristics of the cutter during the rock-breaking process were analyzed in depth. These findings provide a crucial theoretical foundation for the performance design of the new cutter rings, particularly in terms of hardness, toughness, and wear resistance.

The simulations clearly identified the critical role of stress concentration at the cutter-rock interface during the initial stages of rock breaking. During this phase, significant stress concentration was observed at the surface of the cutter in contact with the rock (as shown in Fig. 12). Through simulation analysis, it was found that this phenomenon exacerbates wear, especially at the contact surface between the cutter and the rock. To address this

Material number	C	Mn	Si	S	P	Cr	V	Mo	Fe
S13A	0.51	0.38	0.94	0.004	0.016	5.39	1.04	1.34	Balance
S13B	0.51	0.41	0.93	0.002	0.014	5.28	1.05	1.6	Balance
S13C	0.49	0.3	0.96	0.005	0.015	4.5	0.55	2.95	Balance
S13D	0.53	0.3	0.95	0.03	0.03	5.1	1	1.32	Balance

Table 4. Chemical composition of cutter ring.

Material number	Hardness/HRC	Impact toughness(AKU2/J)
S13A	57.4	21.26
S13B	57.2	15.8
S13C	56.7	13.24
S13D	57.85	20.5

Table 5. Average impact toughness of cutter ring material.

challenge, it is essential to optimize the hardness of the new cutter design. Increasing the material's hardness, particularly by raising the carbon content or using high-hardness alloys, effectively mitigates wear caused by stress concentration and reduces the risk of crack propagation. Therefore, the hardness of the new cutter material must be sufficient to resist localized stress concentration and prevent premature damage.

The simulations also revealed the cyclic loading characteristics that the cutter endures during the rock-breaking process. It was observed that under high-frequency impact loading, the cutter is susceptible to fatigue damage. Particularly in areas with concentrated stress, fatigue cracks may propagate, leading to premature cutter failure. As such, the new cutter material must exhibit excellent fatigue resistance to withstand long-term cyclic loading. The study found that increasing the content of alloying elements, such as nickel and chromium, can enhance the material's fatigue resistance, ensuring the cutter's long-term stability in complex geological conditions.

Finally, wear is a common issue in cutter performance, particularly in high-abrasion formations such as sandstone and sandy mudstone. Cutter surface wear directly impacts cutting efficiency and accelerates cutter degradation. In this context, it is imperative that the new cutter design improves material wear resistance to prolong its service life. Surface reinforcement techniques, such as coating technology, can significantly slow down the wear process. By applying high-hardness coatings to the cutter surface, friction between the cutter and the rock is reduced, thus lowering wear rates and extending the cutter's service life.

Development of a new cutter ring

Development of cutter ring raw materials

Through numerical simulations of the cutter rock-breaking mechanisms and load variations, coupled with the failure analysis of cutter rings in the field, the chemical composition of the cutter ring material was optimized starting from the base material. Commonly used hot-working die steels, such as S13, although possessing certain wear resistance, were found to be insufficient in hardness and toughness after multiple process adjustments. Therefore, based on the hot-working die steel S13, the carbon content was increased (from the original 0.45% to 0.51–0.53%) to enhance the material's hardness. In addition, the proportions of other alloying elements were adjusted to improve the wear resistance and fatigue resistance of the material. Specifically, by increasing the carbon content, the material's hardness was strengthened, allowing it to better resist wear and crack propagation. Furthermore, the contents of chromium (Cr), molybdenum (Mo), and vanadium (V) were optimized. The increase in chromium content improved the material's oxidation resistance and high-temperature performance, while the addition of molybdenum and vanadium further enhanced the material's toughness and wear resistance under high-temperature conditions. The developed materials are designated as S13A, S13B, S13C, and S13D, respectively. Their chemical compositions are shown in Table 4.

Performance analysis of cutter rings

To accurately compare the performance of the four cutter ring materials, each material underwent fast forging and precision forging to produce billets, followed by three-directional deformation ring-rolling for hole expansion. After forming, the rings were subjected to high-temperature spheroidizing annealing and CNC machining into the shape of smooth-edge cutter rings. The specimens were grouped according to the heat treatment process corresponding to each material. After heat treatment, destructive sampling was performed following standard procedures.

The cutter rings were etched using a 4% nitric acid alcohol solution to reveal metallographic features. Hardness tests after heat treatment were conducted using a KH3000 Rockwell hardness tester. Impact test specimens were machined into Charpy U-notch samples measuring 10 mm × 10 mm × 55 mm, and the impact tests were carried out using a JBN-300B impact testing machine.

The average hardness and impact toughness results of the four cutter ring materials are summarized in Table 5. After forging and heat treatment, the hardness of all materials ranged between 56 and 59 HRC; however,

significant differences were observed in impact toughness. Materials S13A and S13D exhibited superior impact resistance and overall mechanical performance. Therefore, S13A and S13D were selected as the raw materials for cutter rings, and the corresponding ring-forging and heat treatment processes were finalized.

Study on surface strengthening processes for cutter rings

Cutter rings require exceptionally high wear resistance and impact resistance. Currently, both domestic and international research efforts are focused on developing new surface-toughening technologies to enhance cutter ring performance. In this study, a nickel-based tungsten carbide powder was selected as the coating material for the cutter ring surface. This type of powder has been widely applied in various surface protection technologies. The nickel-based self-fluxing alloy powder possesses excellent toughness, ensuring that the cutter ring can effectively withstand high impact loads when encountering heterogeneous strata of varying hardness. Meanwhile, by incorporating high-hardness tungsten carbide (WC) ceramic particles into the nickel-based alloy powder, the coating can leverage the superior hardness of WC to reduce continuous abrasive wear from external rock particles on the cutter edge, thereby minimizing cutter ring degradation and significantly extending service life[38].

The fabrication of the wear-resistant cutter ring employed plasma cladding technology[39]. This method offers both economic and operational advantages, with a single cladding layer thickness controllable within 3–6 mm and a relatively high deposition rate. Although the process involves concentrated energy input and substantial impact loads during melting, these drawbacks were effectively mitigated through parameter optimization and process improvements, significantly reducing the formation of defects such as spatter inclusions and cracks. Cutter rings developed using the plasma cladding method not only meet performance requirements but also enhance raw material utilization efficiency. Based on these advantages, a plasma cladding process with a nickel-based WC composite coating was ultimately selected for producing the wear-resistant cutter ring.

Wear resistance testing and analysis of cutter rings

Test principles and procedures

A rotary two-body abrasion test was employed in this study, and the overall testing procedure is illustrated in Fig. 18. The fundamental principle of the test is to evaluate the wear resistance of the cutter ring by measuring the weight loss of the test specimens after frictional contact with the rock surface. The disc-cutter specimens used in the test were extracted from cutter rings made of five different materials. Since the cutter edge is the region directly interacting with the rock, sampling was conducted such that one end of each specimen corresponded to the cutter tooth edge, ensuring consistency between the test conditions and the actual working conditions of the cutter ring. The specimens were cylindrical, with dimensions of φ12 mm × 78 mm. Among all specimens, Specimen 2 was fabricated using the newly developed cutter ring material, whereas the remaining specimens were manufactured using traditional cutter ring materials.

The wear resistance of the disc-cutter specimens was evaluated using the rotary abrasion method, following the "Baron-type steel-rod method for determining rock abrasivity." In the test, the rock block was clamped onto the test bench of the rock abrasivity testing machine, after which the cutter-ring rod was lowered until it made vertical contact with the rock surface. During testing, an axial load of 900 N was applied to the cutter-ring rod. Water cooling was used throughout the process. Each cutter-ring rod underwent at least three abrasion cycles, with each cycle lasting 10 min.

To further investigate the wear resistance of the cutter-ring rods, multiple tests were conducted under varying conditions. Each cutter ring was tested using two to four different rock samples, and the detailed testing scheme is presented in Table 6.

Upon completion of each test, a high-precision balance was used to measure the post-test weight loss of each specimen, which served as the primary indicator for assessing the wear resistance of the cutter rings.

The wear resistance of the specimen is calculated as follows:

$$\alpha = \frac{\sum g_i}{n} \tag{19}$$

where α is the wear resistance of the specimen (mg); n is the number of abrasion cycles performed on a single specimen; and g_i is the mass loss (mg) of the disc-cutter specimen after each abrasion cycle.

Analysis of test results

The wear resistance test results for different rock types are shown in Fig. 19. As shown in the figure, the wear resistance trend of the five specimens is relatively stable. Specimen 2 has the smallest average weight loss. Through the calculation of the relative wear index, we further confirm that the relative wear index of specimen 2 is 1, while the relative wear index of all other specimens is greater than 1, indicating that their wear resistance is relatively poorer than that of specimen 2, with specimen 2 exhibiting the best wear resistance. Additionally, as shown in the figure, under the same conditions, the wear loss of all specimens in the sandstone wear test is generally greater than that in the granite test, suggesting that the hardness of sandstone is lower and its particle roughness is higher, leading to more severe wear. These test results confirm that the newly developed cutter ring material, based on the cutting force mechanics of rock drilling, exhibits superior wear resistance compared to traditional cutter ring materials. However, due to the limited sample size and testing cycles, the current experimental design fails to provide sufficient statistical support. Future studies should increase the sample size and testing cycles to enhance the reliability of the conclusions.

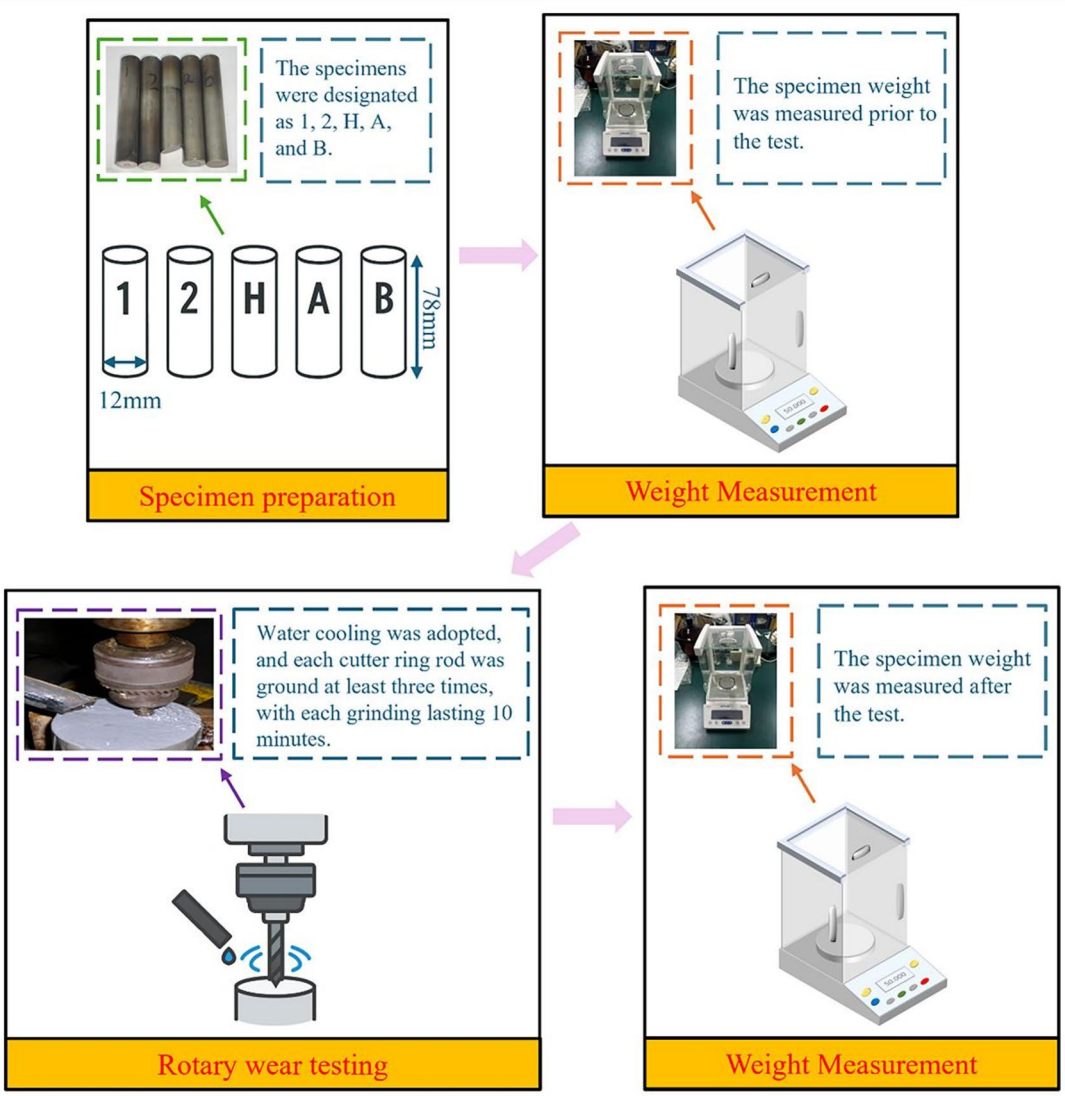

Fig. 18. Experimental procedure for cutter ring wear resistance test.

Specimen	Rock type	Thrust force	Rotational speed
1	Sandstone, Granite	900 N	500 rpm, 710 rpm
2	Sandstone, Granite	900 N	500 rpm, 710 rpm
H	Sandstone, Granite	900 N	500 rpm, 710 rpm
A	Sandstone, Granite	900 N	500 rpm, 710 rpm
B	Sandstone, Granite	900 N	500 rpm, 710 rpm

Table 6. Test scheme of the rotary wear experiment.

SEM analysis of worn surfaces

The primary objective of the scanning electron microscopy (SEM) analysis is to examine, at high resolution, the damage morphology, microstructural changes, and characteristics of wear debris on the metal surface, thereby deepening the understanding of the rock-induced wear mechanisms of disc cutters. After completing the rotary abrasion tests between the cylindrical cutter-ring specimens and the rock using the drilling-type abrasion apparatus, sections were extracted from the cylindrical specimens due to equipment size limitations under adequate test conditions. The section containing the worn cutter-ring surface was preserved for SEM observation. The SEM analysis was conducted using a ZEISS Sigma 360 field-emission scanning electron microscope, as shown in Fig. 20.

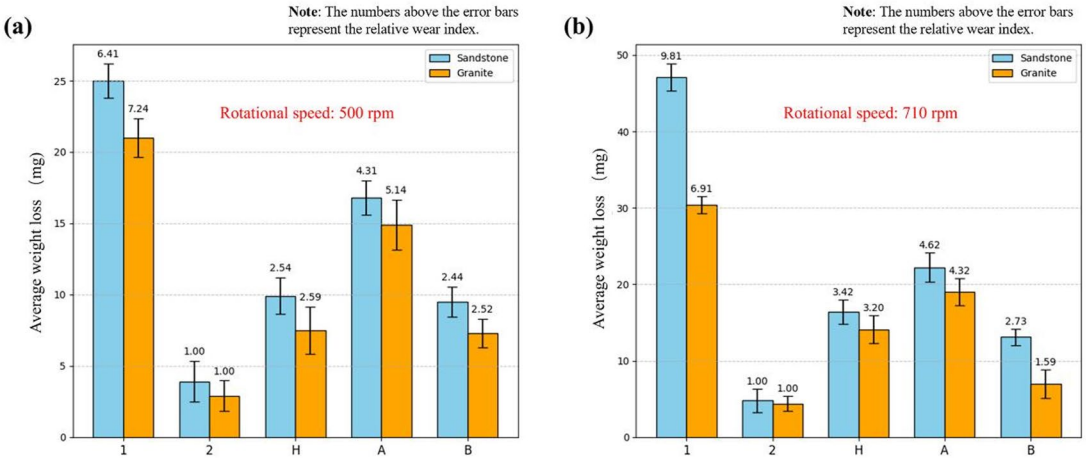

Fig. 19. Rotational wear test results of each specimen: (**a**) rotational speed = 500 rpm, (**b**) rotational speed = 710 rpm.

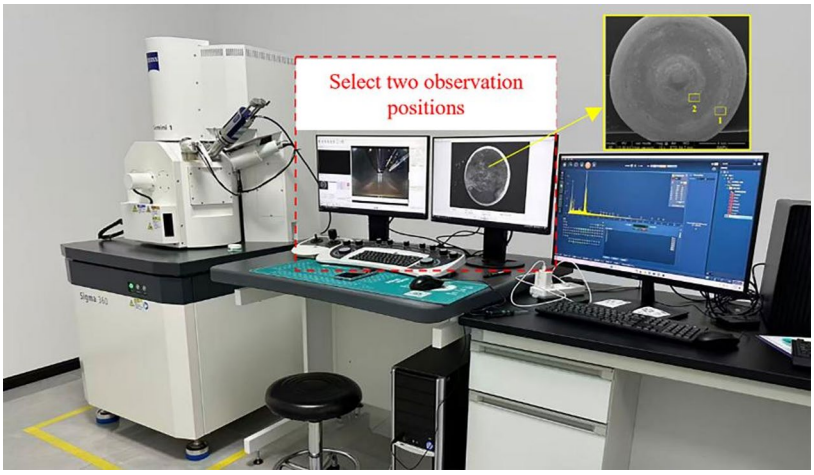

Fig. 20. Environmental scanning electron microscope.

Figure 21 presents the surface morphology of each specimen under macroscopic observation and SEM examination. As shown in Fig. 21a, the macroscopic surface of Specimen 1 exhibits a relatively smooth and flat appearance; Specimen A shows distinct sliding marks; Specimen H also displays a smooth surface, but with noticeable annular abrasion marks; and Specimen B exhibits no pronounced protrusions or pits on the overall worn surface, although several small pits appear in the non-edge region. Overall, among all specimens, Specimen 2 exhibits the smoothest worn surface without visible protrusions or depressions. The macroscopic observations indicate that Specimen 2 possesses higher hardness and better wear resistance, and it may also exhibit more stable chemical behavior, making it less susceptible to environmental interactions during the abrasion process.

As shown in Fig. 21b, examination of the SEM micrographs—taken from two observation planes for each specimen—reveals distinct wear characteristics across the samples. Among them, Specimen 2 demonstrates the strongest wear resistance. In both observation planes, the worn surface of Specimen 2 remains smooth, with uniformly distributed annular scratches and almost no signs of plastic flow, indicating high hardness, excellent wear resistance, and minimal material removal. In comparison, Specimen 1 also shows relatively good wear resistance, with shallow scratches and a generally smooth surface; however, several small white particles and scratches appear in the second observation plane, suggesting the presence of abrasive wear and slightly weaker wear resistance than Specimen 2. Specimen A exhibits numerous irregular scratches and ploughing grooves in the second observation plane, indicating pronounced abrasive wear and noticeable accumulation of hard particles. Although its hardness is relatively high, the worn surface is less uniform than that of Specimen 2 and shows more evident plastic deformation features, reflecting poorer wear resistance. Specimen H presents a relatively rough worn surface with abundant scratches and grooves, as well as unevenly distributed white particles; its surface morphology exhibits strong plastic flow characteristics, suggesting lower wear resistance and more significant plastic deformation. Specimen B shows fish-scale patterns on the worn surface, along

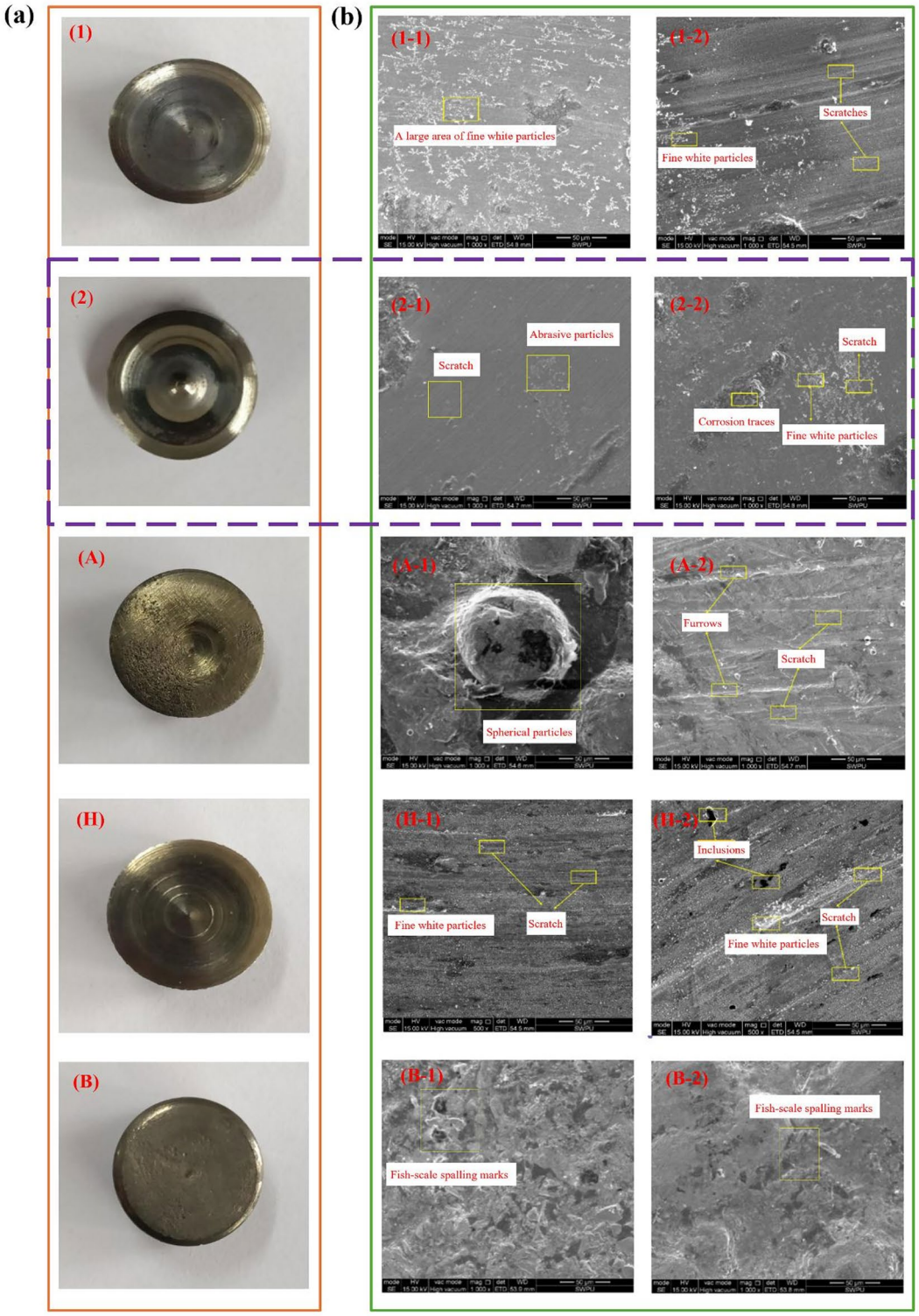

Fig. 21. Observed images of the worn surfaces of all test specimens: (**a**) macroscopic observation images of each specimen, (**b**) micro-scale scanning images of each specimen.

with shallow scratches and relatively good wear resistance, but its abrasion surface is less uniform than that of Specimen 2 and displays more noticeable plastic deformation.

Overall, Specimen 2 exhibits the highest wear resistance and the least surface damage. The other specimens show varying degrees of abrasive wear and plastic deformation, with Specimen 1, Specimen A, and Specimen B demonstrating more pronounced abrasive wear and lower hardness characteristics compared with Specimen 2.

To quantify the wear characteristics of each specimen under both macro and micro observations, profilometer tests were conducted on each specimen. The results showed that the wear depth of Specimen 2 was 0.03 mm, with a surface roughness (Ra) of 1.2 μm; Specimen 1 had a wear depth of 0.06 mm and a surface roughness of 3.5 μm; Specimen A exhibited a wear depth of 0.13 mm and a surface roughness of 5.2 μm; Specimen H showed a wear depth of 0.08 mm and a surface roughness of 3.7 μm; and Specimen B had a wear depth of 0.11 mm and a surface roughness of 4.5 μm. Compared with the other specimens, Specimen 2 demonstrated significant wear resistance and maintained a relatively smooth surface during the wear process.

By analyzing the wear surfaces of each specimen through macro observation, micro observation, and quantitative wear analysis, it can be concluded that Specimen 2 exhibited excellent wear resistance and high hardness. The reason for this superior performance is the higher carbon content and hardness alloying components used in Specimen 2. These elements enhance the material's hardness and wear resistance. The high carbon content not only increases the hardness of the steel but also contributes to its strong wear resistance during the wear process, as higher hardness effectively suppresses plastic deformation and crack propagation. Alloying elements such as chromium and molybdenum further enhance the material's wear resistance and oxidation resistance, particularly in high-temperature and high-friction environments, reducing abrasive wear on the tool surface. Additionally, Specimen 2 underwent high-temperature heat treatment and surface strengthening processes, which further increased the surface hardness and promoted uniformity in the material's internal structure. During the heat treatment process, grain refinement increased the strength and toughness of the material, allowing the cutter to maintain a longer service life under high friction conditions.

Engineering application of the newly developed cutters

To evaluate the performance of the newly developed TBM cutters under the complex geological conditions of Chongqing, field trials were conducted in the section between Huahuiyuan Station and Longxi Station of Bid Sect. "Numerical simulation of rock-breaking by disc cutters in sandstone–mudstone strata" on the Line 4 West Extension Project. The strata encountered in this section primarily consist of sandstone and sandy mudstone. The saturated uniaxial compressive strength of the sandy mudstone ranges from 5.9 to 10.7 MPa, whereas that of the sandstone ranges from 30.3 to 70.4 MPa. Due to the high strength of the sandstone, cutter wear in this section is typically severe.

During the field application, two single-edge disc cutters and two double-edge center cutters developed in this study were installed for trial use. Throughout the entire excavation process, no abnormal cutter wear or premature cutter replacement occurred. The cutters demonstrated long effective excavation duration, and the average wear per ring remained low. Field trial measurements showed that the wear rate of the newly developed cutters was 16–22% lower than that of conventional cutters under similar geological conditions. Specifically, wear was reduced by approximately 18.3% in sandstone formations and about 20.1% in sandy mudstone formations. More importantly, the field trial results demonstrated a significant improvement in cutter service life. In the section between Huahuiyuan and Longxi stations, the number of cutter rings replaced was reduced by about 28% compared to previous operations. For every 120 m of excavation, the average number of cutter rings replaced with the newly developed cutters was 3.2, compared to 4.5 with conventional cutters. This improvement indicates the new cutters' enhanced durability, with fewer replacements and significantly reduced downtime. The field results confirm that the newly developed cutters did not exhibit abnormal failure in medium-hard to hard rock formations and performed excellently in terms of wear resistance and long-term durability, making them suitable for excavation in the sandstone–mudstone composite strata typically encountered in Chongqing.

Conclusions

This study conducted a comprehensive investigation of the rock-breaking behavior and mechanical characteristics of TBM disc cutters under different geological conditions along the University Town South Station–Zhaishanping Station section of Chongqing Rail Transit Line 27. Through numerical simulation and experimental analysis, the study revealed the rock-cutting mechanism in sandstone and mudstone, and systematically evaluated the performance of various cutter types under different lithologies. The findings provide both theoretical support and practical guidance for cutter selection and optimization in TBM tunnelling. The major conclusions are as follows:

(1) A numerical simulation model was established based on ABAQUS, incorporating the Drucker–Prager constitutive model, to analyze the contact stress distribution and crack propagation characteristics between the cutter and different strata. The accuracy of the simulation method was validated by comparing it with wear prediction models and field experimental data. The study reveals that, in hard rock formations such as sandstone, the normal force dominates the rock-breaking process, while in softer strata like mudstone, the rolling force has a relatively minor impact on the breaking process. This research provides theoretical support for optimizing cutter performance in different strata, clarifies the relationship between cutter materials and rock-breaking efficiency, and offers scientific guidance for cutter selection and arrangement in engineering applications.

(2) A comparative analysis of the rock-breaking performance of different cutter types was conducted. The research found that single-edge and double-edge insert cutters exhibit higher cutting efficiency and better wear resistance in hard rocks like sandstone, while smooth-edge cutters show more stable cutting behavior in softer strata like mudstone. By analyzing the mechanical mechanisms during the rock-breaking process, this study revealed the differences in the mechanical characteristics of different cutter types during the initial contact, stable cutting, and transition stages. Notably, in hard rock formations, insert cutters effectively increase cutting force and improve rock-breaking efficiency. Based on these findings, the study provides theoretical support for the optimization of cutter designs, emphasizing the importance of matching cutter

design to geological conditions, and offers practical engineering guidance for cutter selection, cutterhead arrangement, and performance optimization in real-world applications.

(3) Based on the mechanical insights obtained from the numerical analysis, a new cutter-ring material was developed, and surface strengthening processes were introduced to enhance wear and impact resistance. A nickel-based WC composite coating was applied to the cutter-ring surface using plasma cladding, significantly improving abrasion resistance in hard abrasive formations such as sandstone. Experimental testing confirmed that the new cutter-ring material demonstrates superior performance and can significantly extend cutter service life. During the TBM excavation of Chongqing Rail Transit Line 27, the newly developed cutter rings showed no failure modes such as ring cracking or asymmetric wear, confirming their reliability and applicability in complex sandstone–mudstone composite strata.

Although this study provides valuable insights into the mechanical process of rock cutting by the cutter and the development of a novel cutter ring material, several limitations remain. First, the cutting ring was modeled as a linear elastic body, neglecting plastic deformation and fatigue effects, which may lead to deviations from actual conditions, particularly under high-stress and cyclic loading scenarios. Second, while the Drucker–Prager model is commonly used in rock fracture simulations, it does not fully capture dynamic effects during high-speed cutting, where crack propagation may behave differently due to strain rate effects. Additionally, although stress concentration was highlighted in this study, the micro-failure mechanisms of the cutter ring material, such as fatigue crack initiation, were not considered, limiting the design guidance for materials. Lastly, the model simplified rock joints and ignored environmental factors like groundwater, which can significantly affect rock mechanics in real-world conditions. Future research should address these factors, enhance the model's accuracy, and incorporate a larger sample size and more diverse experiments to validate the results and improve cutter tool design.

Data availability

All data generated or analyzed during this study are included in this published article.

Received: 15 December 2025; Accepted: 2 February 2026
Published online: 10 February 2026

References

1. Liu, J. et al. Stress evolution of rock breakages by a disc cutter assisted by pre-cuts. *Arch. Civ. Mech. Eng.* **23**(2), 115 (2023).
2. Ghorbani, E. & Yagiz, S. Predicting disc cutter wear using two optimized machine learning techniques. *Arch. Civ. Mech. Eng.* **24**(2), 106 (2024).
3. Zhou, G. et al. Study on rock-breaking efficiency evaluation of TBM disc cutters based on Rostami prediction equations. *Front. Earth. Sci.* **11**, 1178127 (2023).
4. Zhao, J. et al. Comparison of the specific energies of sinusoidal VCS cutter rings and CCS cutter rings in breaking rock-like materials based on the FEM. *Sci. Rep.* **14**(1), 8142 (2024).
5. Sun, Z. et al. A practical TBM cutter wear prediction model for disc cutter life and rock wear ability. *Tunn. Undergr. Space Tech.* **85**, 92–99 (2019).
6. Jiang, S. et al. Research advances in solvent extraction of lithium: The potential of ionic liquids. *Adv. Funct. Mater.* **35**(29), 2423566 (2025).
7. Li, J. & Zhang, X. Active flow control for supersonic aircraft: A novel hybrid synthetic jet actuator. *Sensors Actuators A Phys.* **302**, 111770 (2020).
8. Zhang, X. & Li, J. Advancements and challenges of high-speed active flow control: Plasma actuators. *Int. J. Heat Mass Transf.* **252**, 127481 (2025).
9. Janc, B., Vižintin, G. & Pal, A. Investigation of disc cutter wear in tunnel-boring machines (TBMs): Integration of photogrammetry, measurement with a caliper, weighing, and macroscopic visual inspection. *Appl. Sci.* **14**(6), 2443 (2024).
10. Gao, C. et al. Study on the influence of TBM disc cutter on the penetration of extremely hard rock in Zijing Tunnel. *Electron. J. Struct. Eng.* **24**(2), 30–37 (2024).
11. Sun, X. et al. Experimental and model investigation on fatigue properties of sandstone after fully coupled thermo-hydro-mechanical cycles. *J. Rock Mech. Geotech. Eng.* **17**, 7931–7949 (2025).
12. Chen, G. et al. Weakening effects of the presence of water on the brittleness of hard sandstone. *Bull. Eng. Geol. Environ.* **78**(3), 1471–1483 (2017).
13. Hu, X. et al. Experiment on rockburst process of borehole and its acoustic emission characteristics. *Rock Mech. Rock Eng.* **52**(3), 783–802 (2018).
14. Cheng, J. et al. Penetration behaviour of TBM disc cutter assisted by vertical precutting free surfaces at various depths and confining pressures. *Arch. Civ. Mech. Eng.* **21**(1), 22 (2021).
15. Yang, C. et al. Numerical investigation of TBM disc cutter cutting on microwave-treated basalt with an unrelieved model. *Arch. Civ. Mech. Eng.* **22**(3), 147 (2022).
16. Zhou, X. et al. Enhanced wear prediction of tunnel boring machine disc cutters for accurate remaining useful life estimation using a hybrid model. *Front. Struct. Civ. Eng.* **18**(4), 642–662 (2024).
17. Shin, Y. J. et al. Machine learning-based prediction model for disc cutter life in TBM excavation through hard rock formations. *Tunn. Undergr. Space Tech.* **150**, 105826 (2024).
18. Su, H. et al. A new prediction model for disc cutter wear based on the principle of dense core-cavity expansion. *Tunn. Undergr. Space Tech.* **165**, 106845 (2025).
19. Lyu, X. et al. Wear prediction and mechanism study of tunnel boring machine disc cutter breaking in hard-soft rock considering thermal effect. *Appl. Sci.* **15**(8), 4183 (2025).
20. Liu, Q. et al. A wear rule and cutter life prediction model of a 20-in. TBM cutter for granite: A case study of a water conveyance tunnel in China. *Rock Mech. Rock Eng.* **50**(5), 1303–1320 (2017).
21. She, L. et al. Prediction of TBM disc cutter wear based on field parameters regression analysis. *Geomech. Eng.* **35**(6), 647–663 (2023).
22. Li, Q. et al. Intelligent identification and warning method of disc cutter abnormal wear in TBM construction based on extreme learning machine. *Sci. Rep.* **14**(1), 30655 (2024).

23. Fang, Y. et al. Effects of driving parameters on TBM dynamic response and cracking of the disc cutter ring: A case study. *Rock Mech. Rock Eng.* **57**(4), 3063–3082 (2024).
24. Zhang, M. et al. Rock-cutting and wear performance of a novel TBM disc cutter with spiral grooves. *Tunn. Undergr. Space Technol.* **129**, 104660 (2022).
25. Chakeri, H. et al. Experimental and numerical investigation of the TBM disc cutter wear using a new tunnel boring machine laboratory simulator. *Heliyon* **10**(17), e37148 (2024).
26. Wang, Q. et al. Development of a rotary cutting test system and drilling experiment for rock mass. *Arch. Civ. Mech. Eng.* **24**(1), 24 (2024).
27. Geng, Q. et al. Numerical and experimental research on the rock-breaking process of tunnel boring machine normal disc cutters. *J. Mech. Sci. Technol.* **30**(4), 1733–1745 (2016).
28. Huang, H., Lecampion, B. & Detournay, E. Discrete element modeling of tool-rock interaction I: rock cutting. *Int. J. Num. Anal. Meth. Geomech.* **37**(13), 1913–1929 (2013).
29. Rostami, J. Performance prediction of hard rock Tunnel Boring Machines (TBMs) in difficult ground. *Tunn. Undergr Space Technol.* **57**, 173–182 (2016).
30. Rostami, J. Study of pressure distribution within the crushed zone in the contact area between rock and disc cutters. *Int. J. Rock Mech. Min. Sci.* **57**, 172–186 (2013).
31. Gertsch, R., Gertsch, L. & Rostami, J. Disc cutting tests in Colorado red granite: Implications for TBM performance prediction. *Int. J. Rock Mech. Min. Sci.* **44**(2), 238–246 (2007).
32. Delaney, B. et al. A contemporary review and data-driven evaluation of Archard-type wear laws. *Appl. Mech. Rev.* **77**(2), 022101–022111 (2025).
33. Archard, J. F. Contact and rubbing of flat surfaces. *J. Appl. Phys.* **24**(8), 981–988 (1953).
34. Hanief, M. & Charoo, M. S. Archard's wear law revisited to measure accurate wear coefficient considering actual sliding velocity. *Mater. Today Proc.* **47**, 5598–5600 (2021).
35. Jiang, H. et al. Comparative study of the rock-breaking mechanism of a disc cutter and wedge tooth cutter by discrete element modelling. *Chin. J. Mech. Eng.* **36**(1), 70 (2023).
36. Lin, L., Xia, Y. & Zhang, X. Wear characteristics of TBM disc cutter ring sliding against different types of rock. *KSCE J. Civ. Eng.* **24**(10), 3145–3155 (2024).
37. Lin, L. et al. Experimental study of the wear behavior of tunnel boring machine disc cutter ring under Fe-based coatings. *Wear* **548–549**, 205361 (2024).
38. Li, X. et al. Effect of WC content on the wear and corrosion properties of oscillating laser-cladding-produced nickel-based coating. *Coatings* **13**(9), 1614 (2023).
39. Liang, G. et al. A study of wear resistance of plasma-sprayed and laser-remelted coatings on aluminium alloy. *Surf. Coat. Technol.* **127**(2–3), 233–238 (2000).

Author contributions

Zuliang Zhong: Writing—review & editing, Supervision, Resources, Project administration, Funding acquisition, Conceptualization. Zhicheng Yang: Writing—original draft, Data curation, Investigation, Formal analysis, Software, Methodology. Xiaoyong Li: Supervision, Resources, Project administration Zhen Li: Supervision, Resources, Methodology. Yiliang Tu: Supervision, Conceptualization, Methodology.

Funding

This study is supported by the Natural Science Foundation of Chongqing Municipal of China (Grant No. CSTB2024NSCQ-MSX0195).

Declarations

Competing interests

The authors declare no competing interests.

Additional information

Correspondence and requests for materials should be addressed to Z.Z.

Reprints and permissions information is available at www.nature.com/reprints.

Publisher's note Springer Nature remains neutral with regard to jurisdictional claims in published maps and institutional affiliations.